



Originally published as:

Lobanov, S. S., Schifferle, L., Schulz, R. (2020): Gated detection of supercontinuum pulses enables optical probing of solid and molten silicates at extreme pressure–temperature conditions. - Review of Scientific Instruments, 91, 5, 053103.

<https://doi.org/10.1063/5.0004590>

Gated detection of supercontinuum pulses enables optical probing of solid and molten silicates at extreme pressure–temperature conditions

Cite as: Rev. Sci. Instrum. **91**, 053103 (2020); <https://doi.org/10.1063/5.0004590>

Submitted: 12 February 2020 . Accepted: 02 May 2020 . Published Online: 18 May 2020

Sergey S. Lobanov , Lukas Schifferle , and Reiner Schulz



View Online



Export Citation



CrossMark

ARTICLES YOU MAY BE INTERESTED IN

[Combination of pulsed light heating thermoreflectance and laser-heated diamond anvil cell for in-situ high pressure–temperature thermal diffusivity measurements](#)



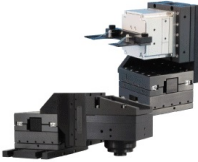
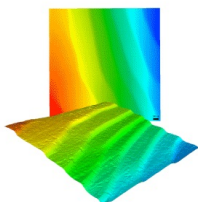
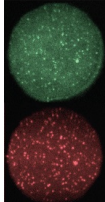
Review of Scientific Instruments **90**, 074901 (2019); <https://doi.org/10.1063/1.5093343>

[X-ray diffraction at the National Ignition Facility](#)

Review of Scientific Instruments **91**, 043902 (2020); <https://doi.org/10.1063/1.5129698>

[CR-39 nuclear track detector response to inertial confinement fusion relevant ions](#)

Review of Scientific Instruments **91**, 053502 (2020); <https://doi.org/10.1063/5.0004129>

 MCL MAD CITY LABS INC. www.madcitylabs.com	<p>Nanopositioning Systems</p> 	<p>Modular Motion Control</p> 	<p>AFM and NSOM Instruments</p> 	<p>Single Molecule Microscopes</p> 
---	--	--	---	--

Gated detection of supercontinuum pulses enables optical probing of solid and molten silicates at extreme pressure–temperature conditions

Cite as: Rev. Sci. Instrum. 91, 053103 (2020); doi: 10.1063/5.0004590

Submitted: 12 February 2020 • Accepted: 2 May 2020 •

Published Online: 18 May 2020



Sergey S. Lobanov,^{a)} Lukas Schifferle, and Reiner Schulz

AFFILIATIONS

GFZ German Research Centre for Geosciences, Section 3.6, Telegrafenberg, 14473 Potsdam, Germany

^{a)} Author to whom correspondence should be addressed: slobanov@gfz-potsdam.de

ABSTRACT

Optical studies of materials at high pressure–temperature (P - T) conditions provide insights into their physical properties that may be inaccessible to direct determination at extreme conditions. Incandescent light sources, however, are insufficiently bright to optically probe samples with radiative temperatures above ~ 1000 K. Here we report on a system to perform optical absorption experiments in a laser-heated diamond anvil cell at T up to at least 4000 K. This setup is based on a pulsed supercontinuum (broadband) light probe and a gated CCD detector. Precise and tight synchronization of the detector gates (3 ns) to the bright probe pulses (1 ns) diminishes the recorded thermal background and preserves an excellent probe signal at high temperature. We demonstrate the efficiency of this spectroscopic setup by measuring the optical absorbance of solid and molten (Mg,Fe)SiO₃, an important constituent of planetary mantles, at $P \sim 30$ GPa and $T \sim 1200$ K to 4150 K. Optical absorbance of the hot solid (Mg,Fe)SiO₃ is moderately sensitive to temperature but increases abruptly upon melting and acquires a strong temperature dependence. Our results enable quantitative estimates of the opacity of planetary mantles with implications to their thermal and electrical conductivities, all of which have never been constrained at representative P - T conditions, and call for an optical detection of melting in silicate-bearing systems to resolve the extant ambiguity in their high-pressure melting curves.

Published under license by AIP Publishing. <https://doi.org/10.1063/5.0004590>

I. INTRODUCTION

Physical properties of crystals and melts in planetary interiors govern large scale geological processes and are central to our understanding of how planets operate and evolve. Transport properties, such as viscosity and electrical and thermal conductivities, are particularly decisive for planetary thermal evolution, magnetic field generation, and mantle convection,^{1–3} but they remain poorly constrained at pressure–temperature (P - T) conditions characteristic of deep planetary interiors. The laser-heated diamond anvil cell (LH-DAC) method,^{4–6} in which a micrometer-sized sample is squeezed between the tips of two diamonds and heated with a laser, provides an important experimental platform for laboratory measurements of physical properties at high P - T . Unfortunately, transport (and other) properties of tiny samples isolated between the anvils are

often inaccessible to direct determination at the P - T conditions of interest. Indirect characterization of transport properties is possible with optical probes that access the sample through the transparent diamonds,^{7–10} but require a tightly focused bright probe to measure the optical response of a hot radiating sample on a small spatial scale ($< 10 \mu\text{m}$ when a near-IR laser is employed for heating).^{11–17} Conventional broadband light sources, such as incandescent light bulbs, allow optical measurements in a wide spectral range but fall short as their brightness is not sufficient to probe samples with radiative temperatures of several thousand Kelvin. This is the main reason why optical studies in DACs that employ conventional light sources are limited to $T \lesssim 1000$ K.^{18,19} Lasers, on the other hand, offer sufficient brightness in a micrometer-sized focal spot but can only probe the sample response (e.g., its absorption coefficient or reflectivity) at a fixed wavelength.¹³ Supercontinuum lasers with broadband

emission and laser-like brightness combine the best of both worlds but require precise synchronization to detector gates due to their intrinsically pulsed output.²⁰ Here we report on a custom LH-DAC setup that combines a supercontinuum light probe synchronized to a gated detector that enabled optical measurements on solid and molten (Mg,Fe)SiO₃ at $P \sim 30$ GPa and up to $T \sim 4150$ K.

II. OPTICAL SETUP

A. General notes

The entire optical setup is realized at the GFZ German Research Center for Geosciences (Potsdam, Germany) on a passive-damped optical table with non-essential components (e.g., power supplies) placed on a custom-built rack atop the table. Within the heating laser path, mirrors, lenses, and beam splitters are compatible with the near-IR laser (i.e., durable and with a high or low reflectivity at the laser heating wavelength). In the probing path, we exclusively use protected silver coated mirrors, which allow for more than 95% reflectance across the entire spectral range of the instrument (450–850 nm). Chromatic aberrations upon light focusing and collection are minimized by the use of achromatic lenses and objectives optimized for the near-IR and visible spectral region.

Spectroscopic measurements are carried out on a dual optical output SpectraPro HRS-300 spectrograph (Princeton Instruments) equipped with three gratings (density: 100 groves/mm, 150 groves/mm, and 300 groves/mm; blaze wavelength: 450 nm, 500 nm, and 500 nm) on a single rotating turret. The direct and side outputs of the spectrograph are occupied by 1024 × 256 RB PI-MAX 4 intensified charge-coupled device (ICCD) and PIXIS-256 CCD (both Princeton Instruments) detectors thermoelectrically cooled to 253 K and 203 K, respectively. The wavelength calibration of the instrument was performed in LightField using the Hg atomic emission of an IntelliCal light source mounted at the entrance slit of the spectrograph. The wavelength calibration accuracy of the

spectrograph is ~ 1 pixel on the CCDs, which translates into 0.3–1 nm depending on the specific grating and detector used for spectral collection.

B. Laser-heating and temperature measurements

For laser heating, we use a continuous wave (cw) 100 W 1070 nm IPG Photonics (YLR-100-AC) Yb fiber laser. The laser (red thick line in Fig. 1) is split into two beams by a polarizing beam splitter (BS) and directed into the 20× Mitutoyo NIR objectives by a pair of dichroic mirrors (DMs). The laser heating power reaching the DAC is controlled by two sets of $\lambda/2$ waveplates (polarization rotation) and polarizing cube beam splitters (dumping of unwanted polarization component) installed upstream from both sides of the DAC. A focal Pi-Shaper positioned upstream relative to the BS allows for a near flat top intensity distribution in the focal plane. Additionally, the Pi-Shaper allows adjusting the diameter of the heating laser beam in the focal plane. In the present work, we used a beam diameter of $\sim 10 \mu\text{m}$, which was small enough for efficient laser heating yet significantly larger than the optically probed spot ($\sim 5 \mu\text{m}$).

Thermal emission of the hot sample is collected from both sides of the DAC and passed through custom-made spatial filters (SFs) each consisting of two achromatic doublets and a confocal 50 μm pinhole, allowing one to spatially select $\sim 10 \mu\text{m}$ in the center of the heated spot. The spatially filtered beams are projected onto the entrance slit of the spectrograph with a vertical offset of ~ 2 mm using a D-shaped mirror, allowing for simultaneous wavelength-dispersed imaging of both sides of the heated sample on a selected detector. The optical response of the thermal radiation collection path was calibrated using a Conrad Electronics halogen lamp positioned between the Mitutoyo objectives. The emission spectra of the laser-heated sample are extracted from non-binned 2D CCD images and fitted in T-Rax²¹ under the graybody assumption. Typically, PIXIS-256 is used for temperature determination at $T < 2500$ K as this detector has a non-zero quantum efficiency at 850–1050 nm, allowing one to

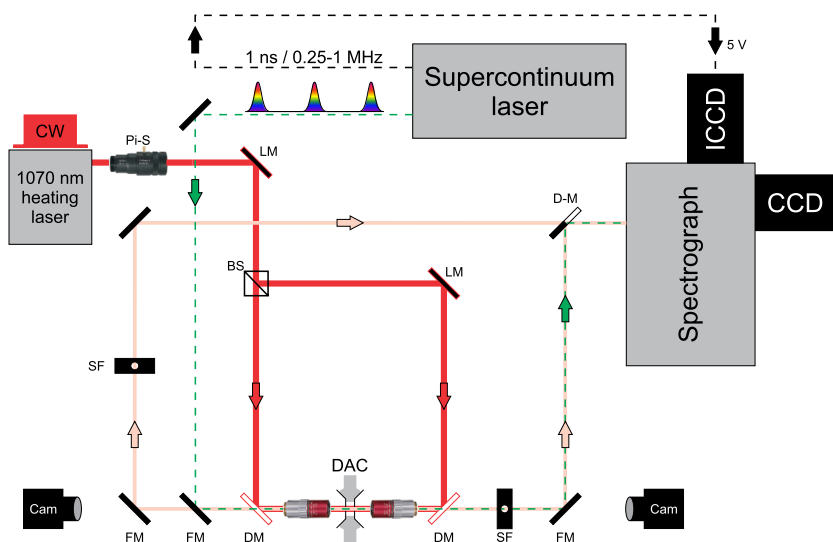


FIG. 1. Simplified optical layout of the LH-DAC instrument. Red arrows depict the heating laser path, pink arrows are for the thermal radiation collection path, and green for the supercontinuum probe path. Pi-S: focal Pi-shaper, LM: laser line mirrors, BS: polarizing beam splitter, DM: dichroic mirrors, DAC: diamond anvil cell, SF: spatial filters, FM: flipping mirrors, D-M: D-shaped mirror, and Cam: observation cameras.

measure temperatures as low as 800 K. On the other hand, the RB intensifier of PI-MAX 4 has essentially zero quantum efficiency at wavelengths higher than 850 nm; thus, it is not well suited for measurements of temperatures below 1300–1500 K. The main benefit of using the ICCD detector is that it offers a factor of $\sim 10^6$ shorter exposures (down to 3 ns) than our PIXIS CCD, making PI-MAX 4 the detector of choice for temperature measurements at $T \gtrsim 2500$ K.

C. Probe-detector synchronization

The probe is a commercially available 2 W Leukos New Wave supercontinuum laser (1 ns pulse width, 0.25–1 MHz repetition rate) and is used without any modifications, providing extreme optical brightness at 400–2400 nm spectral range (full spectrum available at: https://www.leukos-laser.com/site/wp-content/uploads/2019/11/hp_new_wave.pdf). The probe is attenuated by a factor of 10^4 – 10^5 by a set of filters with a neutral optical density (OD) of 4 and 5, respectively, positioned upstream from the DAC. Importantly, most of the probe optical power is in the near-IR range ($\gtrsim 1050$ nm) while our ICCD is insensitive to light with a wavelength of greater than ~ 850 nm. To minimize this unused probe optical power, which may contribute to unwanted sample heating as discussed below, we use a 900 nm short pass filter upstream from the DAC, which reduces the total probe power by a factor of ~ 3 (as measured by a photodiode).

Precise synchronization of the 1 ns probe pulses to shortest possible detector gates of our PI-MAX 4 detector (~ 3 ns) offers the maximum suppression of the continuous thermal background. To achieve precise synchronization, we use the electrical output of the supercontinuum, which goes high every time the laser fires, to trigger a single delayed gating event that records the following probe pulse (Fig. 2). The 3 ns gate width reliably captures the probe as the pulse-to-pulse jitter of the supercontinuum is very small (~ 100 ps). After the single gating event, the detector is set to wait for the next trigger to repeat the gating until a preset number of supercontinuum pulses (typically 50) is accumulated in a single ICCD frame. To improve the signal-to-noise ratio, 100 ICCD

frames are collected, with their average being the end product of a single spectral collection sequence. A laser shutter positioned in the heating laser path upstream from the DAC is synchronized with the ICCD detector to open/close ~ 100 ms prior to/after the spectral collection, which is sufficient to probe a steady thermal state of the sample.²²

D. Comparison to existing setups

The optical layout of our laser-heating instrument is similar to that at the Earth and Planets Division of Carnegie Institution of Washington,²³ but important differences that affect the performance of these instruments exist in the probe-detector synchronization. The setup at Carnegie employs a supercontinuum laser with a 4 ns pulse width synchronized to a 24 ns ICCD gate,¹⁴ while at GFZ (this work) a 1 ns pulse is paired with a 3 ns gate. Accordingly, the setup at GFZ allows for a factor of two more efficient probe-gate overlap in time domain, which translates into a correspondingly smaller contribution of unwanted thermal radiation recorded by the ICCD. In addition, the setup at Carnegie can only catch one in six probe pulses due to the mismatch in probe (250 kHz) and detector (~ 40 kHz) frequencies.¹⁴ At GFZ, the maximum frequencies of the ICCD and the supercontinuum probe are the same (1 MHz) and every probe pulse can be recorded. This is an important advantage of the presented setup as it allows, in principle, for a factor of ~ 25 times shorter laser-heating experiments, helping one to avoid unwanted time-dependent chemical reactions (e.g., iron diffusion). Furthermore, the spectrograph at GFZ houses two detectors (ICCD and a conventional CCD), while the spectrograph at Carnegie only has one optical output (ICCD). The advantage of the setup at GFZ is that the conventional CCD allows for more reliable temperature measurements (especially in the limit of $T \lesssim 1500$ K to 2000 K) because it is sensitive up to ~ 1050 nm (while the ICCD at Carnegie only to ~ 850 nm) and has a smaller dark current (by a factor of $\sim 10^3$) and read noise (~ 2) compared to that of the used ICCD detector.

III. EXPERIMENT

A. Optical absorption measurements at high temperature

Each measurement of an optical absorption spectrum at high temperature involved recording eight different signals (Fig. 3). First, we collected the background (I_{bckg}^{300K}) and the intensity of the probe passed through the transparent pressure medium (I_{ref}) at room temperature. At this step, we maximized the intensity of the supercontinuum laser to obtain the desired number of counts on the ICCD (typically around 60 000). Second, we blocked the probe and adjusted the laser heating power to heat the sample to a desired temperature (T_{before}), taken as an average of the readings from upstream and downstream sides of the sample. This step involved manually switching on the heating laser for about 1–5 s in order to obtain sufficient thermal emission signal on one of the detectors (CCD or ICCD). Once the laser heating power that provides the desired T is found, the heating laser is switched off and the supercontinuum unblocked to collect its transmission through the sample at room temperature (I_{smp}^{300K}). Subsequently, the heating laser is switched on

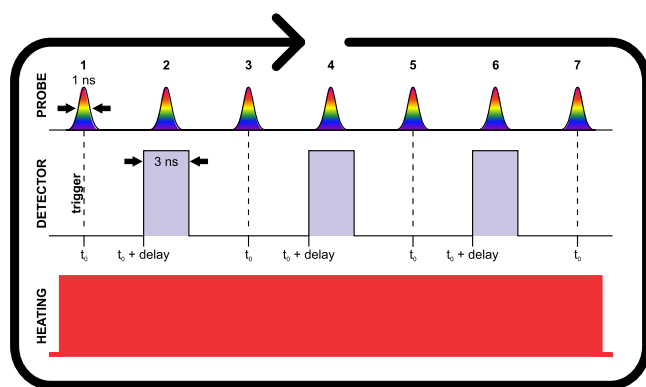


FIG. 2. An example of the probe-detector synchronization. The electrical output of the supercontinuum laser initiates a delayed gating event to collect the following probe laser pulse. The gating is then repeated to accumulate the preset number of laser pulses in a single ICCD frame. The heating laser turns on ~ 100 ms before the first gate and turns off ~ 100 ms after the last one.

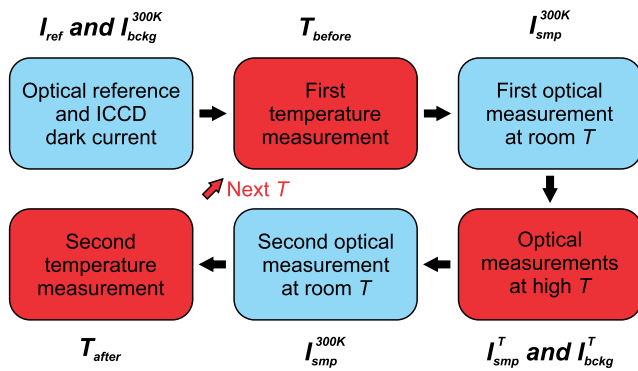


FIG. 3. Experimental sequence used in this work to obtain one high-temperature absorption spectrum.

again to record the probe transmitted through the heated sample (I_{smp}^T). Immediately after this, the probe is blocked and the thermal background (I_{bckg}^T) is measured at identical ICCD exposure and laser heating power. After this step, we repeat the collection of I_{smp}^{300K} as a check on reversibility of sample's optical properties over the optical measurements at high T . Finally, the probe is blocked and the heating laser is switched on to obtain the second temperature measurement (T_{after}). For the results reported here, T_{before} and T_{after} were within 50–100 K and the reported single-value temperatures average these two readings. The temperature values are rounded to the nearest integer, reflecting the statistical uncertainty of the Planck fitting procedure, which was usually within a few degrees. However, overall uncertainty in T is larger²⁴ and is assumed to be within 10% of the reported values. After collecting all necessary signals, we evaluated the sample absorbance at T as $A = -\log_{10}(\frac{I_{smp}^T - I_{bckg}^T}{I_{ref} - I_{bckg}^{300K}})$. The sequence shown in Fig. 3 yields three absorption spectra (pre-, post-, and the high-temperature spectrum). The pre- and post-spectra are room-temperature spectra that test the reversibility over the optical measurements at high T . After processing the absorption spectra, the laser-heating power was adjusted and the sequence of spectroscopic measurements repeated at a different T .

B. DAC loading and sample preparation

A cleaved slab of $(Mg_{0.95}, Fe_{0.05})SiO_3$ glass (prepared by fusing the oxides in pure O_2 gas in an aerodynamic levitation laser furnace) was loaded into a symmetric DAC and the pressure increased to ~30 GPa (measured by the ruby fluorescence method²⁵). The loading involved indenting a Re foil to a thickness of about 40 μm , drilling a circular hole in the center of the indentation, and positioning the sample (~20 μm thick) between two dried KCl wafers (each is ~10 μm thick). Here, we used KCl as a pressure transmitting medium, thermal insulation, and as an independent pressure gauge.²⁶ Prior to optical experiments at GFZ, the glass was compressed to 30 GPa and crystallized at the P02.2 beamline (PETRA III, DESY) by laser-heating the sample and simultaneously measuring x-ray diffraction. Starting from $T \sim 1500$ K, we observed the growth of bridgmanite, the thermodynamic ground state of the $(Mg_{0.95}, Fe_{0.05})SiO_3$ system

at these conditions. At a temperature of ~2000 K to 2200 K, the diffuse signal, which is characteristic of the starting glass material, was no longer present in the x-ray diffraction pattern. The amplitude of the x-ray diffraction peaks of bridgmanite also stopped growing in the same temperature range. Together, these observations indicate full crystallization of the starting $(Mg_{0.95}, Fe_{0.05})SiO_3$ glass. Here it is worth mentioning that bridgmanite inherits the iron content of the starting glass (5 mol. % Fe) because bridgmanite and KCl were the only phases observed in x-ray diffraction after the crystallization. Glass crystallization was repeated at several distinct sample positions to enable independent high-temperature runs for optical measurements at GFZ.

C. Optical absorption spectra at high temperature

Reliable spectroscopic measurements at high temperature require that the thermal background is subtracted accurately from the combined signal recorded by the ICCD (probe + thermal emission). In the present experiments, thermal background was noticeable at the level of a few tens of counts only at $T > 3000$ K with a cumulative exposure of 150 ns (3 ns \times 50 gates). Even at the highest temperature of ~4150 K reached here, the maximum thermal contribution to the total signal measured by the ICCD is ~300 counts [Fig. 4(a)], which together with the T stability over the heating cycle, as indicated by the T_{before} and T_{after} readings, ensures reliable thermal background subtraction [Fig. 4(b)].

It is also important to consider whether the supercontinuum probe itself contributes significantly to the sample temperature. Each pulse of the 2 W supercontinuum laser operated at 1 MHz and attenuated by a factor of 3×10^4 (900 nm short pass + OD4 filter) delivers $\sim 7 \times 10^{-11}$ J to the sample in 1 ns. This is a factor of ~70 smaller than the power delivered by the continuous heating laser ($\sim 5 \times 10^{-9}$ J/ns), which in the present experiments was sufficient to heat the sample to $T \sim 2000$ K. Assuming a wavelength-independent absorptivity of the sample and taking into account the focal plane diameters of the lasers (10 μm vs 5 μm), we obtain that the minimum probe attenuation used in this work may have heated the sample by up to ~100 K, which is within the assumed 10% uncertainty associated with temperature determination. To empirically verify that the supercontinuum does not heat the sample significantly, we compared the optical absorption spectra of $(Mg_{0.95}, Fe_{0.05})SiO_3$ bridgmanite at $T \sim 2500$ K measured by the supercontinuum laser attenuated with the OD4 and OD5 neutral density filters. The resulting absorption spectra were identical. Accordingly, we conclude that within the uncertainties of temperature and absorption measurements, the supercontinuum laser did not heat the samples significantly.

Figure 5(a) plots the optical absorption spectra of our $(Mg, Fe)SiO_3$ sample measured at the same position in the temperature range of $T \sim 1200$ K to 4150 K ($P = 30$ GPa at 300 K). We intentionally refer to the sample chemical composition as $(Mg, Fe)SiO_3$ because of the expected (but not presently quantified) iron partitioning between the solid and liquid samples at $T \gtrsim 3000$ K.²⁷ At ~1200 K $< T \lesssim 1500$ K, bridgmanite is slightly more transparent at 13 000–20 000 cm^{-1} than it is at 300 K due to the decreased intensity of the two Fe^{2+} – Fe^{3+} charge transfer bands (centered at ~14 000 cm^{-1} and ~19 000 cm^{-1}). At $T \gtrsim 1500$ K, however, the Fe–O charge transfer band, which is seen as a UV absorption edge,

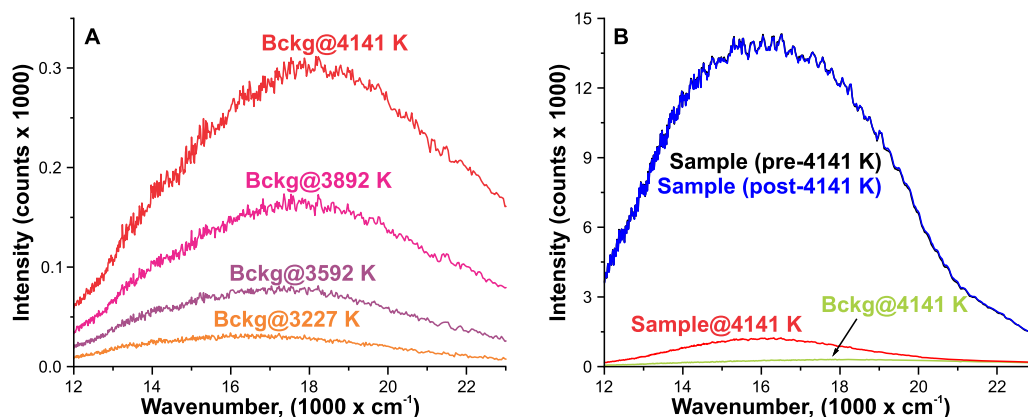


FIG. 4. (a) Examples of thermal radiation off the hot sample ($I_{\text{bckg}}^T - I_{\text{bckg}}^{300\text{K}}$) recorded by PI-MAX 4 with a 150 ns exposure (3 ns \times 50 gates). (b) Probe intensity measured through the sample at 30 GPa just before (black), right after (blue), and upon heating to 4141 K (red) with a total exposure of 150 ns. Thermal background at 4141 K (green) was measured at an identical laser heating power but with the supercontinuum probe being blocked. Note that the probe signals transmitted through the pre- and post-heated samples are identical, indicating that the temperature-induced opacity is fully reversible. Room-temperature background due to the ICCD dark current is subtracted from all the plotted spectra.

takes over due to its continuous temperature-induced red shift and becomes the dominant light absorption mechanism in the visible range. Both these observations are consistent with the previous optical studies of ferromagnesian minerals at $T < 2000$ K.^{14,15,28,29} Importantly, the observed temperature-induced variations in the absorption spectra of bridgmanite are fully reversible at $T \lesssim 2700$ K as evidenced by the virtually identical room-temperature spectra collected prior to the first optical measurement and after the last one (pre-1173 K and post-2708 K spectra in Fig. 5). This apparent reversibility suggests no significant radial iron redistribution within the crystalline sample over all of the heating cycles because absorbance is

sensitive to the iron content. However, we cannot rule out iron diffusion along the laser-heating direction. Future optical studies will need to address this issue by a detailed *ex situ* chemical analysis on the decompressed samples (e.g., transecting the heated spot by a focused ion beam and subsequent mapping by energy-dispersive x-ray spectroscopy).

Optical absorption spectra of solid (Mg,Fe)SiO₃ shown in Fig. 5(a) were measured upon a gradual increase of the heating laser power. In response, the sample temperature increased steadily (300–500 K/1 W) up to the temperature of about 2700 K, which is ~ 250 K below the expected melting T of bridgmanite at 30 GPa.²⁷ However,

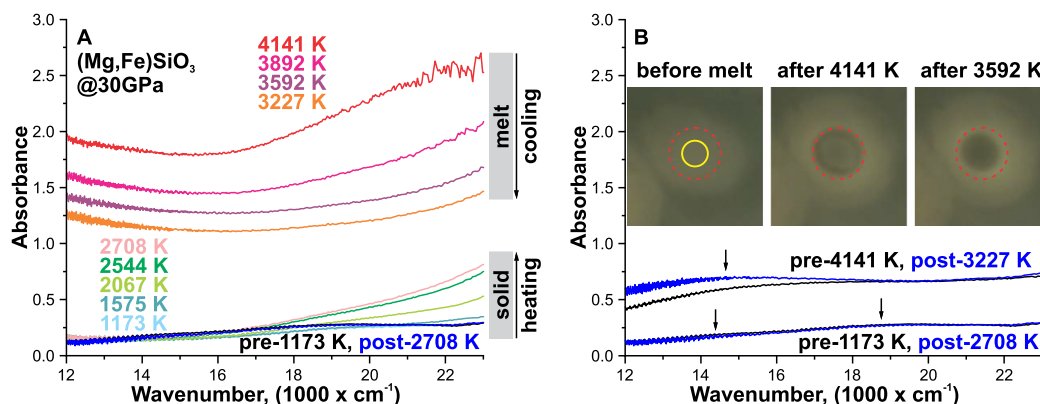


FIG. 5. (a) High-temperature optical absorption spectra of (Mg,Fe)SiO₃ at 30 GPa (~ 18 μm thick). The arrows schematically depict that the optical measurements in the solid/molten sample were performed upon a gradual increase/decrease of the laser heating power. (b) Room-temperature spectra collected just prior to and immediately after the optical measurements at indicated temperatures (1173 K, 2708 K, 4141 K, and 3227 K). Full reversibility over the heating cycles is evident before the first melting event (pre-1173 K and post-2708 K spectra) at $T \sim 3000$ K.²⁷ Arrows indicate the positions of Fe²⁺-Fe³⁺ charge transfer bands. Inset: Microphotographs of the laser-heated spot before the first melting event (left) and after the spectral collections at 4141 K and 3592 K (center and right). Red dashed circles depict the area sampled by the confocal pinhole (~ 10 μm in diameter). The yellow circle is the position of the supercontinuum probe.

a subsequent slight increase in the laser power of ~ 0.2 W resulted in the sample temperature of ~ 4150 K, which is ~ 1200 K above the expected melting T . A circular feature with a dark rim was observed visually in the center of the heated spot immediately after quenching the sample to room temperature [Fig. 5(b), inset], which can be interpreted as the physical boundary of the molten sample at $T \sim 4150$ K.

The sample quenched from $T \sim 4150$ K (the highest temperature reached in the present study) is approximately twice as absorbing as it is prior to the melting [post-2708 K and pre-4141 K spectra in Fig. 5(b)], which is likely due to enhanced light scattering on interfaces (e.g., grain boundaries) generated upon melt crystallization as well as iron partitioning into the melt.²⁷ Despite the increased room-temperature absorbance, the sample at $T \sim 4150$ K is a factor of ~ 10 more opaque than at 300 K [Figs. 4(b) and 5]. Importantly, the radial size of the melt at $T \sim 4150$ K is about twice that of the optical probe [Fig. 5(b), inset]; thus, at this temperature, the entire probe beam traverses the molten sample. This, however, was not necessarily the case for subsequent heating runs to $T = 3000$ – 4000 K (performed upon a gradual reduction of the heating laser power), which must have generated smaller amounts of melt than in the preceding heating to $T \sim 4150$ K. Nonetheless, the high optical absorbance characteristic of the molten sample is evident in all the spectra measured down to $T \sim 3200$ K.

Room-temperature absorption spectra indicate excellent reversibility of the sample's optical properties (within ~ 0.02 absorbance units) over a single high-temperature measurement. This is best illustrated by the identical probe transmissions recorded through the sample just prior to and right after the spectral collection at $T \sim 4150$ K [pre- and post-4141 K signals in Fig. 4(b)]. Despite the reversibility over heating to a given T , the optical absorbance of the quenched sample increased slightly below $\sim 18\,000\text{ cm}^{-1}$ across the entire series of measurements taken while reducing the temperature down to ~ 3200 K [pre-4141 K and post-3227 K spectra in Fig. 5(b)]. This is also seen in the optical images of the quenched samples that appear darker in the central part after melting at $T \lesssim 4150$ K [Fig. 5(b), inset]. These observations are difficult to interpret unambiguously because the central part of the heated spot should be progressively enriched in iron by the succeeding melting events.²⁷ Perhaps, these observations suggest that light scattering in the sample at 300 K is relatively insensitive to the amount of melt generated in the preceding laser heating. Importantly, this scattering does not contribute to the measured absorption spectra of the melt if the melt is homogeneous (free of solid or immiscible particles). *Ex post* analysis of quenched samples will clarify the contribution of light scattering on grain boundaries to the measured absorption spectra.

Overall, the measured temperature dependence of optical absorbance is strong in the partially molten sample ($T \gtrsim 3000$ K) but weak when (Mg,Fe)SiO₃ is in the crystalline state ($T \lesssim 3000$ K). A quantitative estimate of the optical absorption coefficient of molten (Mg,Fe)SiO₃ will require information on the radial and axial overlap of the optical probe with the molten sample, as well as assessing radial and axial thermal gradients within the melt. Absorption coefficients of (Mg,Fe)SiO₃ as a function P - and T - are outside the scope of the present work but will be the focus of our future studies.

IV. POTENTIAL APPLICATIONS

A. Radiative thermal conductivity at high P - T conditions

The geophysical significance of the optical absorption spectra measured at high P - T is that they offer insights into the electronic structure of geomaterials in deep planetary interiors. In the case of bridgmanite, the rapid decrease of the two Fe²⁺–Fe³⁺ charge transfer bands with T suggests a disruption of ferromagnetic interactions between the iron sites, which are responsible for the intensity of these bands.³⁰ The red shift of the Fe–O charge transfer band is likely due to the broadening of the valence and conduction bands (hence, reduced band gap) in the electronic structure of bridgmanite with T . The efficiency of these two light absorption mechanisms controls the overall transparency of bridgmanite in the lower mantle, which in turn determines its radiative thermal conductivity: $k_{\text{rad}} \sim \frac{T^3}{\alpha(v,P,T)}$, where α is the frequency-, pressure-, and temperature-dependent absorption coefficient. Because of its strong temperature dependence, heat conduction by light radiation may be significant in the deep mantle increasing the rate of planetary cooling.³¹ This view has been challenged by previous studies of model ferromagnesian minerals that showed intensification of light absorption in the visible and near-IR range at $T \lesssim 1000$ K at 1 atm^{28,29} but the optical properties of realistic mantle phases have never been measured at appropriate P and T . The experimental setup developed here can be used to delineate α as a function of P and T to eventually settle the debate about the efficiency of radiative heat transport in the mantle.^{17,18,32–34}

B. Electrical conductivity at high P - T conditions

The absorption coefficient of semitransparent materials is also linked to their frequency-dependent optical conductivity: $\sigma(v) = n * \alpha(v) * c * \epsilon_0$, where n is the refractive index, c is the speed of light, and ϵ_0 is the permittivity of free space. One may, in principle, extrapolate the measured optical conductivity to zero frequency in order to obtain the DC conductivity, which in the case of bridgmanite would serve to verify models of mantle electrical conductivity based on geophysical observations.^{35–38} Such an extrapolation, however, is not straightforward as the conductivity of bridgmanite at low frequency is unknown. Nonetheless, the moderate temperature-dependence of absorbance observed here in crystalline (Mg_{0.95}Fe_{0.05})SiO₃ suggests that it remains an insulator at $T \lesssim 2700$ K (at least at $P \sim 30$ GPa), which is in qualitative agreement with direct measurements of bridgmanite electrical conductivity at high P and T .^{39–42} In contrast, strong optical absorptivity of molten (Mg,Fe)SiO₃ suggests that its electrical conductivity may be much higher than that of bridgmanite. This inference is in qualitative agreement with the results of shock compression experiments^{43–46} and *ab initio* simulations^{47,48} that revealed highly conducting silicate melts (albeit Fe-free). Therefore, optical measurements in LH-DAC, such as in the present work, provide an independent check on the alternative techniques used to unravel electrical properties of materials at extreme P - T conditions. Furthermore, the measurements of optical properties at high P - T may be used in tandem with *ab initio* computations of electrical conductivity of materials across a wide-frequency range, yielding more reliable constraints on DC conductivity.³⁴

C. Melting studies at extreme P - T conditions

Reliable constraints on the melting curves of mantle and core materials provide important information on the temperature profile in the present-day Earth.²⁷ For example, the melting curves (solidus and liquidus) of potential mantle materials (e.g., peridotite or basalt) set quantitative bounds on the temperature at the core-mantle boundary because seismic studies indicate that the lowermost mantle is not completely solid.⁴⁹ Previous melting experiments in such systems reported solidus (first melt) temperatures that differ by up to 600 K at the core-mantle boundary pressure of 135 GPa.^{50–52} Many of the previous studies used *in situ* synchrotron x-ray diffraction to detect the first melt. This technique, however, is not particularly sensitive to the appearance of first melt as its fraction in the volume sampled by the x-rays is small. In contrast, detection of the first melt by optical spectroscopy must be very efficient because of light scattering in submicrometer-sized melt pockets^{50–52} as well as iron partitioning into the melt increasing its optical opacity. This potential application is supported by the results of this work (Fig. 5) that show that light absorption in silicates changes abruptly (and irreversibly) upon melting of Fe-bearing bridgmanite. The full reversibility in room-temperature spectra up to $T = 2718$ K suggests that the sample remained solid upon the gradual increase of the laser-heating power up to this temperature. However, the subsequent slight increase in the laser heating power by ~ 0.2 W, which in the sample with gradually changing optical properties would correspond to a temperature increase of 50–100 K, produced an irreversible change in the absorption spectrum and a temperature of over 4000 K. These observations point to a solidus temperature of ~ 2800 K, in reasonable agreement with the estimate available in the literature (~ 2950 K²⁷) for the pressure of ~ 30 GPa. Therefore, the experimental setup presented here holds promise for melting studies of geologically relevant samples with optically based detection of the first melt. In addition, our setup enables *in situ* characterization of the absorption coefficients at high P - T , which are necessary for reliable temperature determination if the sample's optical properties are strongly wavelength dependent.⁵³

DATA AVAILABILITY

The data that support the findings of this study are available from the corresponding author upon reasonable request.

ACKNOWLEDGMENTS

S.S.L. acknowledges the support of the Helmholtz Young Investigators Group CLEAR (Grant No. VH-NG-1325). We thank Monika Koch-Müller for encouraging us to work on this project and James Badro for providing the sample of (Mg,Fe)SiO₃ glass. Technical assistance of Sergio Speziale, Hans-Josef Reichmann, Reik Sünkel, and Wilfried Steiner is also highly appreciated. The authors also thank Jochen Hanf and Norbert Gulde of Teledyne Princeton Instruments for technical support and installation of spectroscopic equipment at GFZ.

REFERENCES

- C. Davies, M. Pozzo, D. Gubbins, and D. Alfè, *Nat. Geosci.* **8**, 678 (2015).
- T. Lay, J. Hernlund, and B. A. Buffett, *Nat. Geosci.* **1**, 25 (2008).
- B. A. Buffett, *J. Geophys. Res.: Solid Earth* **97**, 19581, <https://doi.org/10.1029/92jb00977> (1992).
- L. C. Ming and W. A. Bassett, *Rev. Sci. Instrum.* **45**, 1115 (1974).
- S. Petitgirard, A. Salamat, P. Beck, G. Weck, and P. Bouvier, *J. Synchrotron Radiat.* **21**, 89 (2014).
- G. Y. Shen and H. K. Mao, *Rep. Prog. Phys.* **80**, 016101 (2017).
- A. F. Goncharov, V. V. Struzhkin, and S. D. Jacobsen, *Science* **312**, 1205 (2006).
- A. F. Goncharov, P. Beck, V. V. Struzhkin, R. J. Hemley, and J. C. Crowhurst, *J. Phys. Chem. Solids* **69**, 2217 (2008).
- M. Murakami, A. F. Goncharov, N. Hirao, R. Masuda, T. Mitsui, S. M. Thomas, and C. R. Bina, *Nat. Commun.* **5**, 5428 (2014).
- S. S. Lobanov, A. F. Goncharov, and K. D. Litasov, *Am. Mineral.* **100**, 1059 (2015).
- R. S. McWilliams, D. A. Dalton, Z. Konôpková, M. F. Mahmood, and A. F. Goncharov, *Proc. Natl. Acad. Sci. U. S. A.* **112**, 7925 (2015).
- R. S. McWilliams, D. A. Dalton, M. F. Mahmood, and A. F. Goncharov, *Phys. Rev. Lett.* **116**, 255501 (2016).
- M. Zaghou, A. Salamat, and I. F. Silvera, *Phys. Rev. B* **93**, 155128 (2016).
- S. S. Lobanov, N. Holtgrewe, and A. F. Goncharov, *Earth Planet. Sci. Lett.* **449**, 20 (2016).
- S. S. Lobanov, N. Holtgrewe, J. F. Lin, and A. F. Goncharov, *Earth Planet. Sci. Lett.* **479**, 43 (2017).
- S. Q. Jiang, N. Holtgrewe, S. S. Lobanov, F. H. Su, M. F. Mahmood, R. S. McWilliams, and A. F. Goncharov, *Nat. Commun.* **9**, 2624 (2018).
- S. S. Lobanov *et al.*, *Earth Planet. Sci. Lett.* **537**, 116176 (2020).
- A. F. Goncharov, B. D. Haugen, V. V. Struzhkin, P. Beck, and S. D. Jacobsen, *Nature* **456**, 231 (2008).
- S.-M. Thomas, C. R. Bina, S. D. Jacobsen, and A. F. Goncharov, *Earth Planet. Sci. Lett.* **357–358**, 130 (2012).
- A. Labruyère, A. Tonello, V. Couderc, G. Huss, and P. Leproux, *Opt. Fiber Technol.* **18**, 375 (2012).
- N. Holtgrewe, E. Greenberg, C. Prescher, V. B. Prakapenka, and A. F. Goncharov, *High Pressure Res.* **39**, 457 (2019).
- J. A. Montoya and A. F. Goncharov, *J. Appl. Phys.* **111**, 112617 (2012).
- R. S. McWilliams, Z. Konôpková, and A. F. Goncharov, *Phys. Earth Planet. Inter.* **247**, 17 (2015).
- L. R. Benedetti and P. Loubeyre, *High Pressure Res.* **24**, 423 (2004).
- K. Syassen, *High Pressure Res.* **28**, 75 (2008).
- A. Dewaele, A. B. Belonoshko, G. Garbarino, F. Occelli, P. Bouvier, M. Hanfland, and M. Mezouar, *Phys. Rev. B* **85**, 214105 (2012).
- D. Andrault *et al.*, *Phys. Earth Planet. Inter.* **265**, 67 (2017).
- T. J. Shankland, U. Nitsan, and A. G. Duba, *J. Geophys. Res.* **84**, 1603, <https://doi.org/10.1029/jb084ib04p01603> (1979).
- K. Ullrich, K. Langer, and K. D. Becker, *Phys. Chem. Miner.* **29**, 409 (2002).
- P. A. Cox, *Chem. Phys. Lett.* **69**, 340 (1980).
- A. M. Hofmeister and J. M. Branlund, in *Treatise on Geophysics*, 2nd ed., edited by G. Schubert (Elsevier, Oxford, 2015), p. 583.
- H. Keppler, L. S. Dubrovinsky, O. Narygina, and I. Kantor, *Science* **322**, 1529 (2008).
- A. F. Goncharov, S. S. Lobanov, X. Tan, G. T. Hohensee, D. G. Cahill, J.-F. Lin, S.-M. Thomas, T. Okuchi, and N. Tomioka, *Phys. Earth Planet. Inter.* **247**, 11 (2015).
- S. S. Lobanov, F. Soubiran, N. Holtgrewe, J. Badro, J. F. Lin, and A. F. Goncharov, *arXiv:1909.01438* (2019).
- S. Constable and C. Constable, *Geochem., Geophys., Geosyst.* **5**, Q01006, <https://doi.org/10.1029/2003gc000634> (2004).
- A. Kuvshinov and N. Olsen, *Geophys. Res. Lett.* **33**, L18301, <https://doi.org/10.1029/2006gl027083> (2006).
- F. Civet, E. Thébaud, O. Verhoeven, B. Langlais, and D. Saturnino, *Geophys. Res. Lett.* **42**, 3338, <https://doi.org/10.1002/2015gl063397> (2015).
- A. V. Grayver, F. D. Munch, A. V. Kuvshinov, A. Khan, T. J. Sabaka, and L. Tøffner-Clausen, *Geophys. Res. Lett.* **44**, 6074, <https://doi.org/10.1002/2017gl073446> (2017).

- ³⁹X. Li and R. Jeanloz, *Geophys. Res. Lett.* **14**, 1075, <https://doi.org/10.1029/gl014i011p01075> (1987).
- ⁴⁰T. J. Shankland, J. Peyronneau, and J.-P. Poirier, *Nature* **366**, 453 (1993).
- ⁴¹R. Sinmyo, G. Pesce, E. Greenberg, C. McCammon, and L. Dubrovinsky, *Earth Planet. Sci. Lett.* **393**, 165 (2014).
- ⁴²T. Yoshino, S. Kamada, C. C. Zhao, E. Ohtani, and N. Hirao, *Earth Planet. Sci. Lett.* **434**, 208 (2016).
- ⁴³D. K. Spaulding, R. S. McWilliams, R. Jeanloz, J. H. Eggert, P. M. Celliers, D. G. Hicks, G. W. Collins, and R. F. Smith, *Phys. Rev. Lett.* **108**, 065701 (2012).
- ⁴⁴A. Denoeud *et al.*, *Phys. Rev. Lett.* **113**, 116404 (2014).
- ⁴⁵M. Millot *et al.*, *Science* **347**, 418 (2015).
- ⁴⁶R. M. Bolis *et al.*, *Geophys. Res. Lett.* **43**, 9475, <https://doi.org/10.1002/2016GL070466> (2016).
- ⁴⁷R. Scipioni, L. Stixrude, and M. P. Desjarlais, *Proc. Natl. Acad. Sci. U. S. A.* **114**, 9009 (2017).
- ⁴⁸F. Soubiran and B. Militzer, *Nat. Commun.* **9**, 3883 (2018).
- ⁴⁹Q. Williams and E. J. Garnero, *Science* **273**, 1528 (1996).
- ⁵⁰G. Fiquet, A. L. Auzende, J. Siebert, A. Corgne, H. Bureau, H. Ozawa, and G. Garbarino, *Science* **329**, 1516 (2010).
- ⁵¹D. Andrault, N. Bolfan-Casanova, G. L. Nigro, M. A. Bouhifd, G. Garbarino, and M. Mezouar, *Earth Planet. Sci. Lett.* **304**, 251 (2011).
- ⁵²R. Nomura, K. Hirose, K. Uesugi, Y. Ohishi, A. Tsuchiyama, A. Miyake, and Y. Ueno, *Science* **343**, 522 (2014).
- ⁵³S. S. Lobanov and S. Speziale, *J. Geophys. Res.: Solid Earth* **124**, 12825, <https://doi.org/10.1029/2019jb018668> (2019).